# Carrier trapping and activation at short-period wurtzite/zinc-blende stacking sequences in polytypic InAs nanowires

J. Becker,[1] S. Morkötter,[1] J. Treu,[1] M. Sonner,[1] M. Speckbacher,[1] M. Döblinger,[2] G. Abstreiter,[1] J. J. Finley,[1] and G. Koblmüller[1,*]

[1]*Walter Schottky Institut and Physik Department, Technische Universität München, Garching, Germany*
[2]*Department of Chemistry, Ludwig-Maximilians-Universität München, Munich 81377, Germany*

(Received 28 August 2017; published 22 March 2018)

We explore the effects of random and short-period crystal-phase intermixing in InAs nanowires (NW) on the carrier trapping and thermal activation behavior using correlated optical and electrical transport spectroscopy. The polytypic InAs NWs are grown by catalyst-free molecular beam epitaxy under different temperatures, resulting in different fractions of wurtzite (WZ) and zincblende (ZB) and variable short-period (∼1–4 nm) WZ/ZB stacking sequences. Temperature-dependent microphotoluminescence ($\mu$PL) studies reveal that variations in the WZ/ZB stacking govern the emission energy and carrier confinement properties. The optical transition energies are modeled for a wide range of WZ/ZB stacking sequences using a Kronig-Penney type effective mass approximation, while comparison with experimental results suggests that polarization sheet charges on the order of ∼0.0016–0.08 C/m along the WZ/ZB interfaces need to be considered to best describe the data. The thermal activation characteristics of carriers trapped inside the short-period WZ/ZB structure are directly reproduced in the temperature-dependent carrier density evolution (4–300 K) probed by four-terminal (4T) NW-field effect transistor measurements. In particular, we find that activation of carriers in-between $\sim 10^{16}-10^{17}$ cm$^{-3}$ follows a two-step process, with activation at low temperature attributed to WZ/ZB traps and activation at high temperature being linked to surface states and electron accumulation at the InAs NW surface.

DOI: 10.1103/PhysRevB.97.115306

## I. INTRODUCTION

One of the most intriguing features of III-V semiconductor nanowires (NW) is their peculiar microstructure allowing crystal-phase polytypes to occur which are otherwise not present in the bulk form. While classical bulk III-V semiconductors, like GaAs, InP, etc., are well known to adopt the cubic zincblende (ZB) structure, their NW form can also stabilize the wurtzite (WZ) phase. This is mainly attributed to the small difference in cohesive energy between ZB and WZ structures in the limit of small NW diameters and the modified interface energies as opposed to conventional planar growth [1,2]. Many efforts have been undertaken to realize high-quality, phase-pure III-V NWs of either ZB or WZ phase [3–6]—however, the formation of stacking defects, twins, and uncontrolled mixing of WZ/ZB crystal phases are still the most commonly observed scenario in the majority of III-V NWs [7–10].

Extended investigations have been performed to elucidate the effects of the polytypism on the band structure and band alignment as well as resulting electronic and optical properties of III-V NWs with intermixed ZB and WZ crystal phases. Based on optical studies there is now large consensus that the interfaces of WZ/ZB polytypes of the most common III-V NW materials (GaAs, InP, InAs, etc.) form a staggered type-II band alignment [7,10–15], in good agreement with calculations based on density functional theory [16]. A prominent example for the utilization of the band offsets at individual WZ/ZB interfaces is the realization of crystal-phase quantum dots (CPQD), where charge carrier trapping leads to sharp-line excitonic transitions and single photon emission properties [17–19].

With respect to electrical properties, crystal-phase mixing by WZ/ZB polytypes has been shown to increase resistivity by orders of magnitude and decrease carrier mobility compared to phase-pure NWs as observed, e.g., for InP NWs [14] and InAs NWs grown by various different techniques [20]. Indeed, in InAs NWs – currently considered as promising candidates for future high-speed/low-power electronics [21,22] and investigations of quantum transport phenomena [23,24]–the band offset between WZ and ZB phase is relatively high, which should lead to significant trapping effects of electrons along the NW. Recent experimental data suggest a conduction band (CB) offset in-between ∼95 meV [25] and ∼120 meV [26], which is close to the values predicted theoretically (∼130 meV) [16,27]. The large trapping potential at WZ/ZB-interfaces of InAs NWs has recently been exploited to establish single electron transport at low temperature with clear Coulomb oscillations, as demonstrated in ZB-InAs NWs with well-defined WZ barriers [25]. Moreover, investigations of transistor characteristics showed that InAs NWs with mixed WZ/ZB polytypes also resulted in different pinch-off (current-on/off) behavior as opposed to pure ZB-phase NWs although their intrinsic transport coefficients were very similar [28]. This behavior was attributed to the presence of polarization sheet charges at the WZ/ZB interfaces, which screen the intrinsic electron accumulation at the InAs NW surface and thereby modify

*Corresponding author: Gregor.Koblmueller@wsi.tum.de

 ©2018 American Physical Society

the contact resistance. Polarization-mediated sheet charges arising in InAs NWs with WZ-phase or intermixed WZ/ZB crystal-phase boundaries have recently been investigated by several groups, with values scattering over a wide range from $\sim 10^{-4}\,\mathrm{C/m^2}$ [29,30] to $5\times 10^{-2}\,\mathrm{C/m^2}$ [28,31]. In addition, and closely linked to the understanding of polarization sheet charges, the theoretically predicted CB offset between WZ and ZB phase in InAs was recently also verified by experiments [30].

Despite the vast progress made in correlating the structural properties of mixed-polytype InAs NWs with respect to their electronic band structure and electrical conductivity data, there are some remaining questions to be solved: first, most investigations of electrical conductivity relied on two-terminal (2T-) measurements of NW-field effect transistor (NW-FET) devices, which do not account for changes in contact resistance with variable crystal phase [20]. As a result, reported electrical conductivity data do not specify purely the *intrinsic* NW carrier conduction. In addition, previous investigations compare NW material from various different growth sets, where variations in background carrier concentration due to different growth methods and growth parameters can be fairly high with densities reaching well above $10^{18}\,\mathrm{cm^{-3}}$ [20,28,32–34]. Under such high unintentional doping, contributions from impurities may affect carrier trapping via Coulomb screening, thus obscuring the activation/de-activation processes of carriers confined at WZ/ZB crystal interfaces [20,35,36]. The carrier activation processes are further believed to be influenced by the intrinsic surface states and electron accumulation at the InAs NW surface [20,35,37,38]. In this regard, an unambiguous assignment of the individual contributions to carrier activation mediated by potential barriers at the WZ/ZB interfaces or by surface states remains to be shown. Given the complexity in deriving carrier trapping and activation from electrical transport measurements alone, it would be, therefore, desired to simultaneously evaluate the carrier trapping behavior also by other independent and contactless methods, e.g., optical spectroscopy. This would not only allow us to gain direct insights into the carrier confinement at the WZ/ZB phase boundaries, but also facilitate a more straightforward discrimination between different contributions to the carrier trapping potential.

In this work, we perform a combined photoluminescence (PL) spectroscopy and electrical transport study of the carrier trapping and thermal activation processes at WZ/ZB interfaces in polytypic InAs NWs with different crystal stacking sequences. The InAs NWs studied here were grown by noncatalytic (i.e., droplet-free) solid-source molecular beam epitaxy (MBE), representing a class of NWs that crystallize predominantly in a WZ-dominated phase with random polytype intermixing [39–41] and residual background carrier concentrations typically lower than achieved by other methods [37,42]. In particular, we focus here on a set of InAs NWs with different ratios between WZ and ZB stacking and different average segment lengths as realized by varying growth temperature. Temperature-dependent micro-PL ($\mu$PL) and four-terminal (4T-) back-gated NW-FET measurements were used to extract distinct differences in the carrier trapping for different WZ/ZB stacking order, which are independent of contact resistance and also account for the presence of polarization sheet charges in these NWs. The combined advantages given by the directly correlated optical-electrical approach, the 4T-device geometry, the careful selection of NWs with otherwise nearly identical parameters (NW diameter, carrier concentration) allow us to clearly pin down structure-mediated changes in intrinsic NW conductivity and carrier trapping behavior.

## II. EXPERIMENTAL DETAILS

The growth of the intrinsically $n$-type InAs NWs was performed in a solid-source Gen-II MBE system equipped with standard effusion cells for group-III elements (Al, Ga, In) and a Veeco valve cracker cell supplying arsenic ($As_4$). As substrates we used Si (111) wafers covered with a ∼2–5-nm-thick, RF sputtered and wet chemically etched $SiO_2$ layer, which served as a mask for nucleating NWs in a selective-area like fashion from random nm-sized pinholes [43,44]. As a result, InAs NWs grew vertically well-aligned along the epitaxial [111]-orientation (i.e., (0001) in WZ notation) in an entirely noncatalytic process without the formation of self-catalyzed droplets and without tapering [43]. In recent work, we found that under this noncatalytic growth mode the NWs can be grown within a fairly large growth window, i.e., growth temperatures of ∼400 °C–580 °C and V/III flux ratios (As/In ratios) of ∼4–60 [44]. In the present study, we depict a growth series under fixed V/III ratio (As/In ∼34 given by In ∼0.24 Å/s, As ∼8.1 Å/s) but variable growth temperatures of $T^{\mathrm{G}} = 430\,^{\circ}\mathrm{C}$, 490 °C, and 530°C, since growth temperature appears to have the largest influence on tuning the crystal phase and stacking sequences as further shown below. All growths were performed for 120 min, resulting in NW lengths of ∼1.8–4.0 $\mu$m and NW diameters of ∼70–150 nm, whereby the longest NWs were obtained for intermediate temperature of $T^{\mathrm{G}} = 490\,^{\circ}\mathrm{C}$ in accordance with Ref. [44]. A summary of the NW dimensions as obtained from scanning electron micrographs (SEM) and other growth related parameters are depicted in Table I.

For each sample we conducted transmission electron microscopy (TEM) investigations on NWs transferred onto carbon-coated copper grids using a JEOL JEM 2011 operating at 200 kV. Both diffraction patterns and high-resolution TEM images were recorded in a ⟨10–10⟩ zone axis corresponding to the side facets of the NWs in the WZ notation. This is important since for other zone axes pointing in other directions one may not distinguish between WZ and ZB structures. During TEM analysis, the size of the selected area diffraction (SAD) aperture was adjusted to the full length of the NW to gain representative diffraction pattern information of the whole NW. To provide statistically significant data, we characterized ∼5–7 NWs from each sample where we found no qualitative differences among individual NWs within a given sample.

The $\mu$PL experiments were performed in a home-built setup for spectroscopy in the infrared (IR) spectral range. A helium/neon (He/Ne) laser was used for excitation, while the emitted PL signal was detected by a liquid-$N_2$ cooled InSb photodiode detector. Hereby, the as-grown, vertically freestanding InAs NW arrays were probed in a He-flow cryostat kept under vacuum, where temperature-dependent measurements between 4 and 300 K were enabled by a temperature controller. The excitation laser spot size focused onto the sample had a spot diameter of ∼2 $\mu$m, corresponding to an

TABLE I. Summarized data of the three investigated samples, specifying growth temperature ($T^G$), NW length ($L_{NW}$), and diameter ($D_{NW}$) as obtained from a statistical analysis of >20 NWs/sample using scanning electron microscopy, as well as average segment lengths of 3C-ZB and 2H-WZ segments in each sample. Also, the density of different types of stacking faults (I1,I2,E) are given as well as the total fraction of hexagonal vs cubic stacking. The structural data were obtained from HR-TEM analysis of ∼50-nm long sections probed at random positions along several NWs per sample.

| | $T^G$ (°C) | $L_{NW}$($\mu$m) | $D_{NW}$(nm) | ZB length (nm) | WZ length (nm) | I1 (1/$\mu$m) | I2 (1/$\mu$m) | E (1/$\mu$m) | hex / cub (%) |
|---|---|---|---|---|---|---|---|---|---|
| A | 430 | 2.5 ± 0.84 | 90 ± 12 | 1.7 ± 0.2 | 1.7 ± 0.1 | 423 | 200 | 63 | 52 / 48 |
| B | 490 | 4.2 ± 0.49 | 86 ± 7 | 0.9 ± 0.2 | 2.3 ± 0.2 | 382 | 124 | 31 | 71 / 29 |
| C | 530 | 1.8 ± 0.20 | 117 ± 17 | 0.8 ± 0.1 | 3.4 ± 0.3 | 217 | 71 | 23 | 81 / 19 |

excitation volume of ∼50–80 NWs per sample. Importantly, all parts along the optical excitation path and the detection side were purged with dry nitrogen to reduce absorption from the surrounding ambient [10].

To characterize the electrical transport properties back-gated NW-FETs were fabricated by dispersing as-grown NWs onto heavily doped $n^{++}$-Si (100) substrates covered with 200-nm thick $SiO_2$ and large Ti/Au contacts (24 bond pads) prepatterned by optical lithography. The NWs were then contacted individually by a set of Ni/Au (20 nm/80 nm) contacts using electron beam lithography (EBL), placing a total of four contact fingers onto each NW to realize 4T-transport measurements. A typical example of a contacted NW-FET is shown below in the next section. Prior to metal contact deposition, the native oxide of the NWs as well as residual impurities were removed using an ammonium fluoride/buffered hydrofluoric (2% conc.) acid mixed with deionized water (ratio 1:2). No thermal annealing of the Ni/Au contacts was performed prior to the measurements. Note that the inner contacts are placed as far apart from each other (at least >350 nm) to increase the channel length and fully suppress any screening effects of the applied gate bias via fringing capacitances that would decrease the transconductance of the device [45]. Temperature-dependent 4T measurements were performed down to 4.2 K in a He-4 flow cryostat where the NW-FET samples were mounted to custom-made chip carriers using wire bonding. In order to discriminate between NW resistivity and contact resistance, the *dc* voltage ($V_{SD}$) was applied to an outer contact and the respective current $I_{SD}$ was measured between the outer lying source and drain contacts, whereas the voltage drop due to the intrinsic NW resistivity was measured via the inner probe contacts (H,L). After electrical characterization all NW-FETs were probed by SEM to measure the diameter and length of the NW channel required to determine the gate capacitance.

## III. RESULTS

### A. Structural properties

Figure 1 shows representative diffraction patterns together with characteristic HR-TEM images for the three investigated InAs NW samples grown at different temperatures. It is obvious that the microstructure depends very sensitively on the selected growth temperature, exhibiting a transition from highly disordered crystal stacking at low temperature (430 °C) to a more distinct WZ stacking at higher temperatures (490 °C and 530 °C). More specifically, for the NWs grown at $T^G = 430$ °C the SAD pattern [Fig. 1(a)] evidences largely continuous streaks, which illustrate the underlying stacking disorder. Because of the overall random stacking, it is difficult to clearly distinguish between ZB or WZ sensitive reflections in the SAD pattern. These characteristics are also evidenced in the associated TEM image [Fig. 1(b)], showing that the stacking changes randomly every few monolayers (ML). A closer look at the HR-TEM of Fig. 1(c) enables, however, further insights into the individual stacking sequences, evidencing that the few-ML wide stacking variations are associated to very short-period polytypes. In particular, we are able to assign these short-period segments to either the cubic (3C) ZB polytype (composed of "ABC" stacking sequences) or the hexagonal (2H) WZ polytype (with "AB" stacking), where each letter corresponds to a bilayer (one pair of atomic layers) of vertically stacked In and As atoms. For the assignment of distinct 3C-ZB and 2H-WZ polytype segments our criterion was that at least four consecutive bilayers of the same stacking sequence should be present within a segment (i.e., a minimum of ABCA for ZB and ABAB for WZ) [39,46]. When counting the individual bilayer sequences in the TEM images over a statistically large enough length along several NWs, we obtain a variation in the length of 3C-ZB and 2H-WZ domains between ∼1.4–1.9 nm and ∼1.5–1.8 nm, corresponding to average segment lengths of 1.7 ± 0.2 nm for each domain, respectively (see Table I). In general, there are also other polytypes such as the 4H ("ABCB") and 6H ("ABCACB"), which have larger unit cell than the 2H-WZ polytype and by their mixed hexagonal/cubic character are found occasionally at transition boundaries from 3C-ZB to 2H-WZ structure in NWs [47]. From the criteria above, we cannot discriminate 4H- and 6H-polytypes in the present NWs since their stacking sequences are too short (typically less than one unit cell), and hence we treat such layer sequences with mixed cubic/hexagonal character rather as stacking defects. To this end, we can identify three different types of stacking faults (SF) when using the WZ crystal structure as basis, i.e., two intrinsic (I1,I2) and one extrinsic (E) SF. Insertion of one *cubic* layer in otherwise hexagonally stacked layers denotes the I1-SF (ABA*B*CBC), insertion of two cubic layers defines the I2-SF (ABA*BC*ACA), while the extrinsic SF is characterized by three cubic layers within a hexagonal basis (ABA*BCA*BAB) [48] (see also Table I). Evaluating the total number of cubically versus hexagonally stacked layers, we can further estimate their respective fractions, which amount to ∼50% each for the NW sample grown at $T^G = 430$ °C.

In contrast, for higher growth temperatures of $T^G = 490$ °C and 530 °C, the SAD patterns [Figs. 1(d) and 1(g)] show the presence of distinct WZ-sensitive reflections (i.e., $01\bar{1}2$ and $0\bar{1}12$ as marked by orange and green arrows), which become more prominent with increasing temperature. Simultaneously,

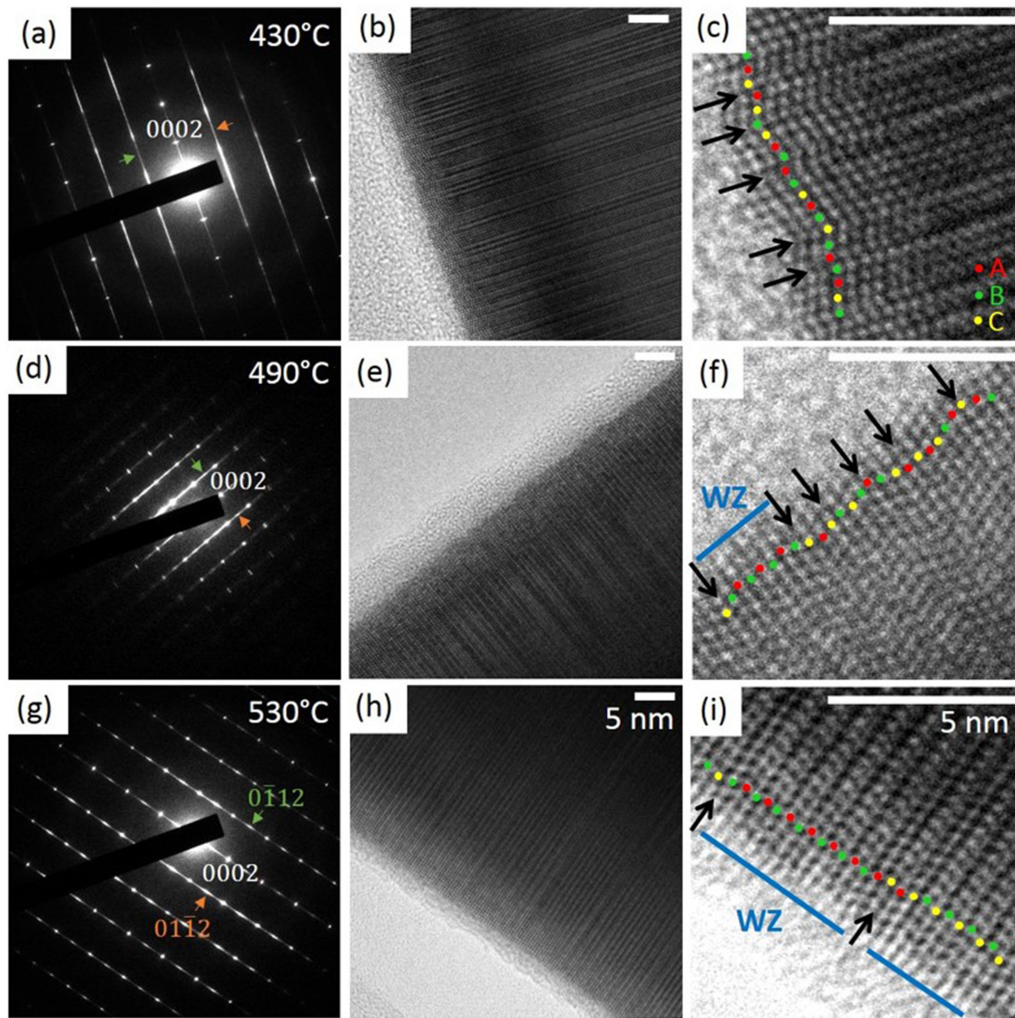


FIG. 1. (a) Selective area diffraction (SAD) patterns and representative HR-TEM images of InAs NWs grown at three different temperatures of [(a)–(c)] $T^{G} = 430\,^{\circ}$C, [(d)–(f)] 490 °C, and [(g)–(i)] 530 °C. WZ sensitive reflections $01\bar{1}2$ and $0\bar{1}12$ are marked by orange and green arrows, respectively, and are clearly visible in all SAD patterns—except for the InAs NW grown at the lowest $T^{G}$ that exhibits continuous streaks signifying the heavily disordered stacking. The HR-TEM images (center and right hand columns) show the characteristic layer stacking, where clear, distinguishable WZ segments are marked in blue and stacking defects by arrows. The layer stacking is also labelled in "ABC" notation, facilitating identification of ZB-type and WZ-type stacking. The scale bar for all images is 5 nm.

the streaks parallel to the growth direction become weaker in intensity, indicating that the frequency of stacking defects is reduced with rising growth temperature. Likewise, the corresponding HR-TEM images illustrate that the random stacking disorder diminishes and WZ-type "AB" stacking becomes more dominant. While the WZ-phase segment lengths did not exceed ~1.8 nm in NWs grown at $T^{G} = 430\,^{\circ}$C, these segment lengths increase up to ~3.5 nm (on average ~2.3 ± 0.2 nm) at $T^{G} = 490\,^{\circ}$C and further to ~5 nm (on average ~3.4 ± 0.3 nm) at $T^{G} = 530\,^{\circ}$C. Simultaneously, the average length of the cubic layer inclusions decreases to ~0.9 ± 0.2 nm at $T^{G} = 490\,^{\circ}$C and ~0.8 ± 0.1 nm at $T^{G} = 530\,^{\circ}$C (see Table I). Since the lengths of these cubic inclusions are smaller than the full 3C-ZB unit cell, the NWs grown at the higher temperatures can hence be understood as having WZ structure with a large density of SFs. As depicted in Table I, the densities of all three types of SFs decrease with increasing growth temperature, while the I1-type is the most dominant SF, followed by the I2- and E-type. This trend is also reflected by the different fractions of hexagonally versus cubically stacked layers, with the WZ-fraction reaching ~70% for $T^{G} = 490\,^{\circ}$C and ~80% for $T^{G} = 530\,^{\circ}$C. We also performed TEM analysis on NWs grown at $T = 580\,^{\circ}$C (not shown here) which exhibited even longer WZ segment lengths (up to > 10 nm), confirming the observed trend towards more WZ-dominated NWs with increasing growth temperature. However, due to the strongly altered axial and radial growth rates [44] such high-$T$ grown NWs could not complement comparable NW aspect ratios required for the present study.

We note that the observation of highly disordered, short-period ZB/WZ stacking at low temperature and higher WZ-phase content at higher temperature is entirely independent of the NW diameter. This was verified from a reference series grown under the exactly same growth conditions and temperatures but with shorter growth times, leading to NW diameters in between 40–60 nm. Such independence of microstructure

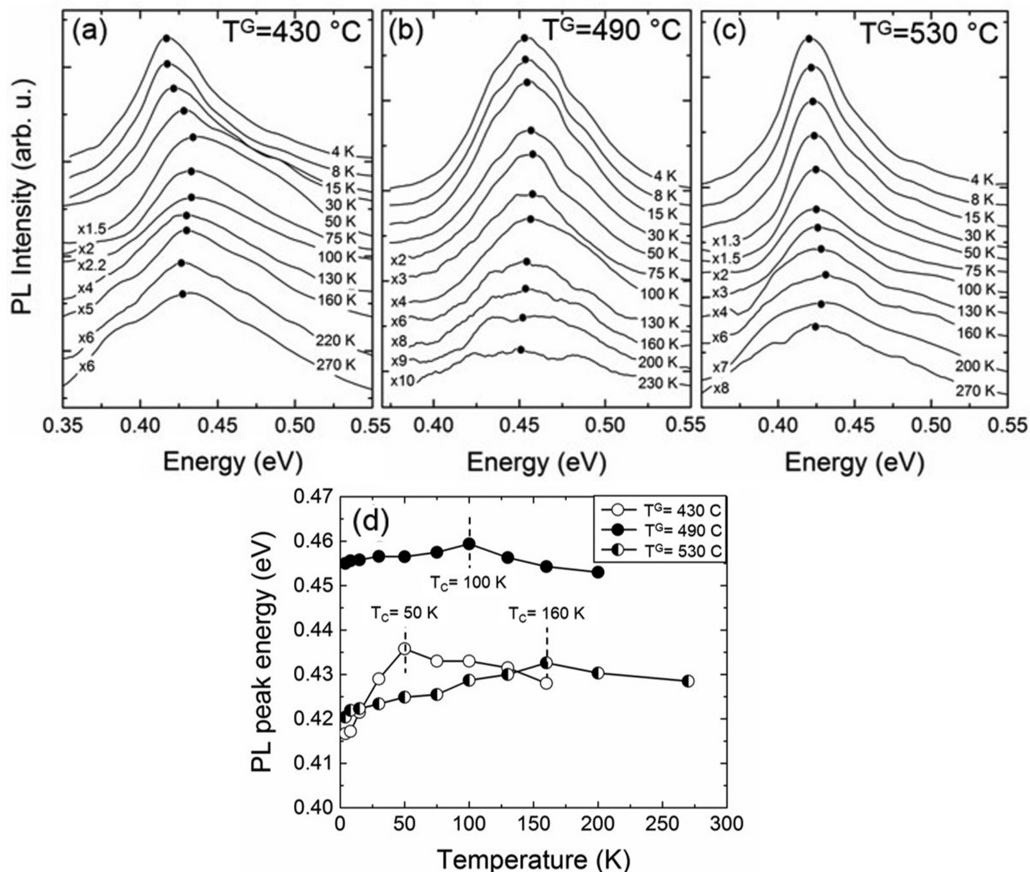


FIG. 2. Temperature-dependent PL spectra as measured for NW arrays grown at (a) $T^{\mathrm{G}} = 430\,^{\circ}\mathrm{C}$, (b) $490\,^{\circ}\mathrm{C}$, and (c) $530\,^{\circ}\mathrm{C}$, at a fixed excitation power of 3.35 mW; (d) PL peak energy as a function of temperature, illustrating a consecutive blue/redshift with increasing temperature; the critical temperature ($T_{\mathrm{c}}$) for the transition between blue- and redshifted PL increases as the growth temperature of the NWs is increased.

from NW diameter appears to be a fundamental property of the underlying noncatalytic growth mode, since it was also observed for MOCVD-grown InAs NWs over an even wider diameter distribution [49]. This is in strong contrast to the more widely studied catalytic, i.e., vapor-liquid-solid (VLS) grown InAs NWs, where commonly narrower diameters yield WZ phase and wider diameters ZB phase [46,50,51]. In VLS-grown NWs thermodynamic effects (i.e., Gibbs-Thomson effect) and nucleation at the triple phase boundary have significant impact on the formation of different crystal phases and stacking defects, which can be tuned by size effects [50]. Furthermore, the thermodynamic models which are also frequently used to explain variations in microstructure with growth temperature in VLS-grown NWs, i.e., via modifications of catalyst nucleus-interface energies and liquid alloy supersaturation [2,3,52–54], cannot be employed for the present non-catalytic NWs. We therefore suggest that for noncatalytic NW growth the driving forces for crystal-phase modifications are more likely kinetic effects, such as temperature-induced changes in adatom surface concentration and reconstruction [55,56]. Although no systematic reports have been conducted on InAs NWs before, stacking defect densities were indeed found to decrease with increasing growth temperature as found in e.g., (111)B-oriented noncatalytic GaAs NWs, which was attributed to reconstruction-mediated changes in surface energy [56].

### B. Optical properties

To characterize the influence of the different WZ/ZB stacking on the carrier trapping and activation behavior among the three samples, we performed temperature-dependent $\mu$PL spectroscopy. Figure 2 shows representative PL spectra obtained from the three samples for temperatures ranging from 4.2 to 270 K. All spectra reveal PL peak energies that are above the band gap value of the phase-pure ZB phase of InAs for any given lattice temperature [10]. This confirms the overall WZ-type character of the investigated NWs—note, the pure WZ phase of InAs has a band gap value that is ∼40–60 meV higher than the phase-pure ZB phase [16,26,57]. The PL peak energies are, however, still below the band gap of WZ-InAs, which is consistent with the widely accepted model that in polytypic III-V nanowires the transition energy is governed by carrier localization due to the type-II band alignment between WZ and ZB domains [7,10–15].

Interestingly, we observe that the PL peaks do not continually shift to higher energies with increases in the WZ character of the NW structure. Instead, comparison of the three sets of spectra shows that the NWs grown at the highest temperature ($T^{\mathrm{G}} = 530\,^{\circ}\mathrm{C}$), which exhibits the largest WZ-phase fraction, have a lower peak emission energy (by ∼20–30 meV) than NWs with less hexagonal character, i.e., NWs grown at $T^{\mathrm{G}} = 490\,^{\circ}\mathrm{C}$. This indicates that it is *not* the overall fraction of WZ versus ZB phase that governs the PL emission properties, but

TABLE II. Summarized transport data of the three investigated NW samples, specifying growth temperature ($T^G$), carrier density at 300 K, the critical temperature for carrier activation (transition between regions *I* and *II*) in comparison with that obtained by PL [$T_C$(PL)], as well as the extracted activation energies for carrier activation from the two prominent traps associated with WZ/ZB interfaces ($E_A^I$) and surface defect states ($E_A^{III}$).

| Sample | $T^G$(°C) | $n$(cm$^{-3}$) 300 K | $T_C = T_I - T_{II}(K)$ | $T_C$(PL) (K) | $E_A^I$(meV) | $E_A^{III}$(meV) |
|---|---|---|---|---|---|---|
| A | 430 | $3.5\times10^{17}$ | 60 | 50 | $4.6 \pm 0.5$ | $39 \pm 2$ |
| B | 490 | $2\times10^{17}$ | 130 | 100 | – | $62 \pm 2$ |
| C | 530 | $1\times10^{17}$ | 160 | 160 | – | $192 \pm 32$ |

rather the nature of the WZ/ZB stacking (e.g., period, segment length) and the corresponding confinement potential. In order to provide an understanding for this behavior and illustrate how the different WZ and ZB segment lengths influence the optical transition energies, we provide a discussion below that also includes a generic model of an idealized homogeneous WZ/ZB polytype structure.

To further illustrate the carrier localization effects due to the WZ/ZB intermixing, Fig. 2(d) plots the evolution of the peak energy as a function of lattice temperature. For all investigated NW samples we identify an anomalous blueshift/redshift of the luminescence peak energy with increasing temperature (often referred to as "*S-shape*" behavior) instead of the monotonous band gap shrinkage, i.e., Varshni-type redshift, for ideally perfect semiconductors [58]. This anomalous S-shape character is a signature of the localized states originating from potential variations due to WZ/ZB mixed stacking in III-V based NWs as observed previously in polytypic InAs and GaAs NWs [10,59]. Note that the S shape, particularly the critical onset temperature ($T_C$) for the final redshift related to band gap shrinkage, varies between the different NW samples. For example, for NWs with the heaviest polytype structure and shortest-period WZ/ZB stacking ($T^G = 430\,^\circ$C), the critical temperature $T_C$ is at around ~50 K. This temperature increases with larger WZ segment lengths, i.e., $T_C \sim 100$ and ~160 K for NW grown at $T^G = 490\,^\circ$C and 530 °C, respectively (see also Table II). The increase in the critical onset temperature illustrates clearly that carriers require larger thermal activation to overcome the barriers induced by the CB offset between ZB and WZ stacking. Remarkably, this carrier activation behavior is directly reproduced also in temperature-dependent electrical transport measurements, as further illustrated in the next section.

### C. Electrical transport properties

To independently study the dependence of the stacking variations on the carrier trapping and activation behavior using other approaches, temperature-dependent electrical transport measurements were performed on 4-terminal NW-FET devices as illustrated in Figs. 3(a) and 3(b). As mentioned before, the 4T-device geometry allows us to separate intrinsic NW conductivity from NW contact resistance, which is important to establish comparison of data unobscured by contacting effects. It is noteworthy that the room-temperature contact resistances ($R_C$) of the devices shown in the following vary with microstructure, i.e., they increase from $R_C = 7.8\,\text{k}\Omega$ ($T^G = 430\,^\circ$C) to $R_C = 16.4\,\text{k}\Omega$ ($T^G = 490\,^\circ$C) and to $R_C = 61.5\,\text{k}\Omega$ ($T^G = 530\,^\circ$C), respectively, i.e., yielding up to one order of magnitude higher contact resistance for InAs NWs with higher WZ-phase fraction. This trend agrees well with previous findings by S. Dayeh, *et al.* [28]. Figure 3(c) depicts the intrinsic NW conductivity as a function of gate voltage $V_g$ based on exemplary transfer characteristics of a single NW-FET device, as fabricated from NWs grown at $T^G = 430\,^\circ$C and measured in the temperature range between 295 and 6.2 K. The device was measured in a gate voltage range of $-10\,\text{V} \leqslant V_g \leqslant 10\,\text{V}$ with multiple sweeps using a source-drain bias voltage of $V_{SD} = 0.5\,\text{mV}$. Overall, the device shows only minimal hysteresis (5.4$\mu$S or 0.97 V around $V_g = 0\,\text{V}$) at room temperature, while at lower temperature hysteresis was completely absent. Therefore, in Fig. 3(c), we

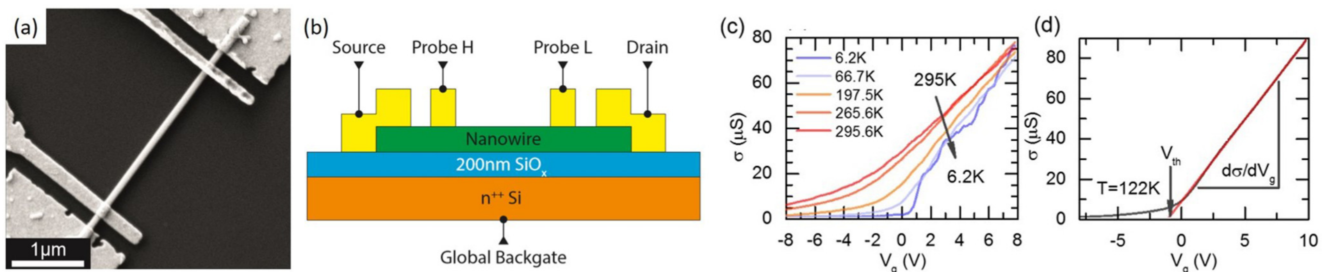


FIG. 3. (a) Scanning electron micrograph and (b) schematic illustration of a typical InAs 4T-NWFET. The four terminals consist of individual Ni/Au contacts for source and drain (outer contacts) and inner probe contacts (H,L), while the n$^{++}$−Si substrate serves as a global backgate. (c) Temperature-dependent transfer curves (conductivity $\sigma$ vs $V_g$) from an InAs NW grown at $T^G = 430\,^\circ$C. (d) Typical transfer curve of the same device (recorded at 122 K) depicting the linear regression of the conductivity and extraction of threshold (pinch-off) voltage $V_{th}$ from the intersection with the $V_g$ axis.

present only the up-sweep part of the transfer curve, which is representative of the transport characteristics. The device confirms the expected intrinsic $n$-type carrier conduction of the InAs NWs, given the increase in conductivity with increased positive $V_g - V_{th} > 0$. We also observe that while the transfer curves are relatively smooth at temperatures >50 K, steplike features are superimposed on the pinch-off characteristics for lower temperatures (e.g., see trace at 6.2 K). These features might be signatures of the depopulation of quasi-1D subbands and an indication for quantum-confined transport in the NW channel [24,60].

Most importantly, the data further show a continuous shift in the threshold voltage $V_{th}$, i.e., pinch-off, towards more negative gate voltages with increasing temperature. Note that the threshold voltage is defined by the linear regression of $\sigma = g_m(V_g - V_{th})$ and the intersect with the $V_g$ axis, where $g_m$ denotes the transconductance ($g_m = d\sigma/dV_g$), as illustrated in Fig. 3(d). The threshold voltage is a very useful metric, as it is directly correlated with the carrier density in the NW channel. The charge carrier density ($n$) can therefore be derived, when considering the charge balance between the charge of the gate capacitor ($Q$) and the accumulated charge ($n$ e) in the device channel, i.e., $C_g V_{th} = Q = ne\,l\,A$, where $C_g$ is the gate capacitance, $l$ and $A$ are the length and cross-section area of the NW channel, respectively. Hence the carrier density amounts to $n = C_g V_{th}/(e\,l\,A)$ and requires an estimate of the gate capacitance of the given device. Here, we calculated the gate capacitance based on the convenient metal plate capacitor model suggested by Wunnicke *et al.* [61], which approximates the back-gated NW-FET by a plate capacitor with a hexagonally shaped NW on top of the $SiO_2$ gate dielectric. In this approximation, the gate capacitance is given by $C_g = (2\pi\varepsilon_0\varepsilon_r l)/\cosh^{-1}(1 + h/r)$, where $\varepsilon_r \sim 2.25$ is the effective dielectric constant for this configuration, while $h$ and $r$ denote the distance between the metal plate and the center of the NW (approximate thickness of the $SiO_2$ gate dielectric) and the radius of the NW, respectively. The calculated gate capacitance for the NW-FET shown in Fig. 3 is 55 aF, while values for $C_g$ of all investigated NW-FETs are in the range of ~11–80 aF.

Figure 4(a) shows the calculated carrier density $n$ as a function of temperature for the same NW-FET as recorded in Fig. 3, i.e., from sample A grown at $T^G = 430\,^\circ$C. From the temperature dependence it is obvious that the carrier density decreases with decreasing temperature by approximately one order of magnitude, i.e., from $\sim 3.5\times10^{17}\,\mathrm{cm}^{-3}$ at 295 K to $\sim 5\times10^{16}\,\mathrm{cm}^{-3}$ at 6K. Very similar carrier densities, both as absolute values as well as relative changes with temperature, were observed also for several other NW-FETs fabricated from the same sample. We note that the room-temperature carrier density value compares favorably with other catalyst-free, MBE-grown InAs NWs reported in the literature [37], and is overall lower than typical carrier densities obtained in, e.g., MOCVD (metal organic chemical vapor deposition)-grown InAs NWs, which are prone to large carbon impurity incorporation [28,32,34,62]. For the other two investigated samples ($T^G = 490\,^\circ$C and 530°C), the carrier densities at room temperature are found to be slightly smaller, i.e., $\sim 2\times10^{17}\,\mathrm{cm}^{-3}$ and $\sim 1\times10^{17}\,\mathrm{cm}^{-3}$, respectively (Table II). The slight change in carrier density between the respective samples suggests that

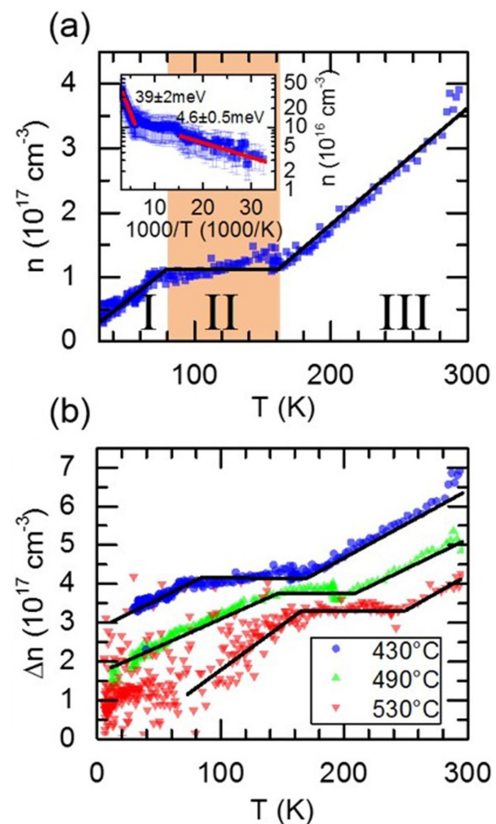


FIG. 4. (a) Temperature dependence of $n$-type carrier density of a representative InAs NW from the sample grown at $T^G = 430\,^\circ$C. The inset shows an Arrhenius plot illustrating two specific regions for carrier activation, i.e., at low temperature ($E_A^I \sim 4.6$ meV) and at high temperature ($E_A^{II} \sim 39$ meV) with activation energies obtained form best fits to the data. Error bars are due to the uncertainties in extracting the threshold voltage $V_{th}$ during pinch-off. (b) Comparison of the temperature-dependent carrier density from NWs grown at the three growth temperatures $T^G = 430\,^\circ$C, 490 °C, and 530 °C, which exhibit different WZ/ZB stacking order and hence different thermal carrier activation characteristics. Solid lines represent guides to the eye. For ease of comparison, we plot here not the absolute carrier density but the relative change in carrier density for each sample.

polytypic InAs NWs with longer WZ segments and reduced stacking defects result in decreased carrier densities as opposed to NWs with more frequent WZ/ZB intermixing and larger number of stacking faults (compare Table I). Still, even though the present MBE-grown InAs NWs are undoped, their carrier densities are much higher than what is expected from pure intrinsic semiconductor material. In fact, purely nondegenerate semiconducting behavior in InAs is expected only for carrier densities below $n \sim 10^{14}\,\mathrm{cm}^{-3}$ [62,63], as defined by the Mott transition [64], i.e., the transition between degenerate metal-like conduction and non-degenerate semiconducting behavior. Hence the carrier densities of our present InAs NWs are ~2–3 orders of magnitude higher than the carrier density defined by Mott's transition, indicating that they should exhibit a degenerate (metal-like) behavior. In ideal degenerate semiconductors, no thermal activation is required to excite carriers into the conduction band, and, thus, the carrier density typically remains unchanged with temperature.

In contrast to the classical behavior of bulklike degenerate semiconductors, the InAs NWs exhibit, however, a very distinct temperature dependence despite the high carrier density. In fact, the temperature dependence can be divided into three characteristic regimes as delineated in Fig. 4(a), i.e., region *I* at low temperature, region *II* at intermediate temperature, and region *III* at high temperature. While region *II*, extending from ~50 to 170 K, exhibits constant carrier density typical for degenerate behavior, region I (<50 K) and region *III* (>170 K) show characteristic carrier activation upon variable temperature [see Fig. 4(a)]. To evaluate the thermal activation more closely, we plotted the inverse temperature dependence (Arrhenius plot) of the carrier density on a logarithmic scale (see inset). By fitting the linear slope of regions *I* and *III* according to $\sim\exp(-E_A/k_BT)$, we obtain insights into the strength of the carrier activation process and the nature of the underlying carrier traps for the two respective activation processes. Specifically, best fits to the data at low temperature yield an activation energy of $E_A^{I} = 4.6 \pm 0.5$ meV, while for the high-temperature region we obtain $E_A^{III} = 39 \pm 2$ meV. We propose that the two distinct activation processes arise from two different kinds of potential barriers (traps) within the NW that carriers need to overcome during transport. At this point, we tentatively associate the thermal activation of carriers at low temperature to potential barriers induced by the WZ/ZB band offset, since the respective carrier activation follows closely the same trend observed in the temperature-dependent PL emission properties. On the other hand, activation of carriers that requires much higher temperature (and hence higher activation energy) is considered to be linked to surface states and related surface electron accumulation on the $\{2\bar{1}\bar{1}0\}$ InAs NW sidewalls [65]. In the following, we provide additional experiments that further help the understanding of the nature of the two different thermal activation processes in more detail.

First, we analyzed the temperature-dependent charge carrier conduction also for NW-FETs fabricated from NW samples grown at $T^G = 490\,^\circ$C and 530°C. The temperature dependence of the respective carrier densities is shown in Fig. 4(b) together with that for NWs grown at $T^G = 430\,^\circ$C. Several interesting trends can be observed when comparing the three different samples. Notably, the carrier activation at low temperature (region *I*) is extended towards higher temperatures with increasing growth temperature before the carrier density starts to saturate (region *II*). Note that the critical temperature for the transition from region *I* to region *II* is $T_C \sim 60$ K (for $T^G = 430\,^\circ$C), $T_C \sim 130$ K (for $T^G = 490\,^\circ$C), and $T_C \sim 160$ K (for $T^G = 530\,^\circ$C), reproducing almost exactly the same thermal activation behavior as observed by PL in Fig. 2(d) (see also Table II). Since the critical temperature $T_C$ shifts to higher temperatures for samples grown at higher $T^G$, this suggests that the barriers for electrons that need to be overcome become larger as the WZ-phase fraction and segment length increase. This direct correspondence between PL and transport data provides clear evidence that in the low-temperature region the nature of carrier activation is most likely related to the WZ/ZB trapping potential, since the emission energies in PL and their temperature evolution are a direct manifestation of carrier localization at mixed WZ/ZB polytype interfaces [7,10–15,59].

Conversely, surface states, e.g., donor-type states [66] that induce surface band bending and confinement potentials for electrons, and which were previously discussed as possible sources for carrier traps in InAs NWs [20,35,37,67], cannot be made responsible for carrier activation at low temperature. This is because surface states on InAs NWs induce centers for nonradiative recombination [68], and, as such, do not contribute signatures in the observed PL transitions. Rather, surface states may play a role in carrier activation at higher temperatures, i.e., corresponding to region *III* of the thermal activation behavior seen in Fig. 4. We like to note here that for this high-temperature region intrinsic bulk conduction could also be considered but is ruled out, because the measured activation energies (several tens of meV, Table II) are substantially lower than the band gap energy of bulk InAs.

There are several reasons that suggest that this second high-temperature process may be associated with carrier activation related to surface states and the intrinsic electron accumulation on the InAs surface. On the one hand, the temperature-dependent carrier freeze-out behavior is similar to well-known planar III-V materials with high donor-type surface state densities, e.g., InAs and InN [69–72]. Specifically, temperature-dependent Hall effect measurements of InAs and InN thin films exhibit a parallel conduction channel at the surface due to excess surface electrons, which alter the bulklike carrier freeze-out behavior and further provide clear evidence for donor-type surface states inducing potential barriers for carrier conduction up to high temperatures [71]. In analogy, we expect the high donor-type surface state densities on the $\{2\bar{1}\bar{1}0\}$ sidewalls of InAs NWs [38,65] to act in similar ways on carrier activation. The effects should be particularly prominent in thinner NWs, since surface states govern transport in the limit of small-diameter InAs NWs [32,62], as we directly confirm below in Fig. 5.

In Fig. 4(b), we illustrate the effect of the anticipated surface states on the carrier activation in dependence of the different WZ/ZB stacking. In particular, we find that with increasing WZ fraction the onset for activation shifts to higher temperatures, indicating that the band bending and charge

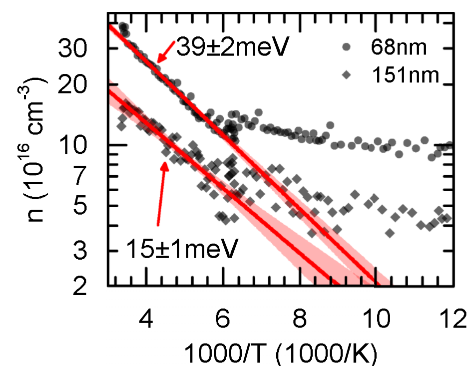


FIG. 5. Inverse temperature dependence of carrier density (Arrhenius plot) as obtained from two NWs with different diameter (68 nm, 151 nm) from sample A ($T^G = 430\,^\circ$C), illustrating the different activation energies in the high-temperature region. Best fits to the data (red lines) clearly demonstrate higher activation energy for the thinner NW.

balance at the NW surface is modified by changes in stacking order. This is also reflected in the respective activation energies (see Table II), which increase from $E_A^{III} = 39 \pm 2$ meV for sample A ($T^G = 430\,^\circ$C) to $E_A^{III} = 62 \pm 2$ meV for sample B ($T^G = 490\,^\circ$C), and to $E_A^{III} = 192 \pm 32$ meV for sample C ($T^G = 530\,^\circ$C). In order to explain this tendency, we suggest that due the different WZ/ZB fractions in the three respective NW samples, the position of the surface Fermi level and the respective surface state density changes. In WZ-dominated InAs NWs, Fermi level pinning at the surface occurs at ∼0.2 eV above the CB minimum [65], which is larger than for NWs with a more ZB-dominated fraction [38]. As a result, surface band bending is expected to be higher in NWs with a larger WZ-phase fraction, which in turn requires increased thermal activation.

Figure 5 further verifies the assignment of surface states to the high-temperature carrier activation process by comparing the behavior of NWs with significantly different diameters. In order to make a valid comparison, we selected NWs only from one specific sample (i.e., sample A) where the WZ/ZB stacking is similar. The data shown in Fig. 5 depicts an Arrhenius plot of the high-temperature region for two NWs with diameters of 68 and 151 nm. As expected, the NW with smaller diameter exhibits larger carrier density due to the more substantial contribution of the surface electron accumulation layer to the transport [32,62]. Concurrently, the stronger influence by the surface electron accumulation layer results in a larger apparent activation energy ($E_A^{III} = 39 \pm 2$ meV) as compared to the NW with larger diameter ($E_A^{III} = 15 \pm 1$ meV). This behavior mimics very closely recent thickness-dependent studies of $n$-type InN films, which evidenced steady increases in the high-temperature slope of the activated carrier density with decreasing thickness due to the stronger influence by surface electrons [72]. We wish to emphasize that the activation energies given here do not represent the activation energy of the anticipated donor-type surface state, but rather show the different relative strengths of the electron accumulation layer on the carrier density. Hence we cannot provide information about the origin of the surface states. Extracting the energy level of the donor-type surface state and its activation energy would require systematic analysis of the temperature-dependence of the pure electron accumulation layer itself, separated from the parallel conduction path through the bulk of the NW.

## IV. DISCUSSION

One of the important findings of the previous section was that the carrier localization properties, as seen in the evolution of the PL emission energies as well as by the carrier activation via transport analysis, varied significantly as a function of the underlying microstructure. Essentially, the data suggested that the confinement potential for carriers are strongly governed by the nature of the WZ/ZB stacking (e.g., period, segment length), which is the main parameter that is varied between the investigated samples. In the following, we propose a model that aims to help the understanding how the WZ/ZB stacking and the respective variations in segment lengths influence the confinement potential and corresponding optical transition energies. This model is based on a previously established concept for polytypic GaAs NWs [73], where the heavy and random polytype sequences are approximated by an idealized periodic WZ/ZB polytype structure. Although this approximation may not reproduce the exact form of the confinement potential and resulting transition energy, it displays very useful guidelines for describing the trends in controlling the optical transition energies via modifications of the WZ/ZB stacking sequences [73]. In addition, we extend this model and also incorporate the effects of polarization sheet charges occurring at WZ/ZB interfaces, which further helps to explain the trends seen in the experimental data.

In our model, we performed calculations of the optical transition energies based on an effective mass approximation (Kronig-Penney type model) using the commercial Schrödinger-Poisson solver NEXTNANO$^3$ [74]. Hereby, we approximated an infinite array of short-period polytype WZ/ZB stacking sequences by a periodic WZ/ZB polytype superlattice consisting of ten SL periods with periodic boundary conditions. Using a simple one-dimensional (1D) calculation, we first calculate the type-II conduction-band (CB) and valence-band (VB) profiles for different ZB and WZ segment lengths using band offset values between WZ- and ZB-InAs as obtained by Bellabes *et al.* [29] ($\Delta E_C = 126$ meV, $\Delta E_V = 56$ meV). Electron and hole effective masses for ZB and WZ phases were also adapted from Ref. [29]. For simplicity, internal strain due to slightly different lattice constants between the mixed WZ and ZB layers was not directly taken into account. However, the effect of strain is considered indirectly by assuming the presence of polarization sheet charges at WZ/ZB interfaces, which arise from piezoelectric (strain-induced) as well as spontaneous polarization fields [30]. Also, in first-order approximation, the calculations neglect the exciton binding energy, which is expected to be less than 1 meV in type-II InAs-based quantum wells due to the spatially separated electron-hole pairs [75].

In Fig. 6(a), we show a three-period section of the calculated conduction and valence band edges for three different SLs which employ the average WZ and ZB segment lengths as provided in Table I. This way the CB and VB profiles tend to approximate the different microstructures obtained from the three investigated NW samples. In this idealistic picture, no polarization sheet charges along the WZ/ZB interfaces are yet taken into account, hence, as expected, the band profiles are entirely flat. Based on the computed band alignments, we further calculated the lowest (highest) lying eigenstates for electrons (holes) confined in each SL structure and their respective squared wave functions (color-coded along the ground states), which are also depicted in Fig. 6(a). The charge density distribution of the electron and hole wave functions clearly illustrates the type-II nature of the WZ/ZB band alignment. From the respective electron and hole ground states, we derived the interband optical transitions based on the electron/hole wave-function overlap. We have performed this for each of the three short-period polytype SL structures at a lattice temperature of 75 K, and compare the calculated transition energies with the experimentally measured PL peak energy at the same temperature. To further illustrate the variation in the transition energies for different WZ and ZB segment lengths, we performed calculations also for WZ segment lengths varying between 1–10 nm and ZB segment lengths of 0.8 and 1.7 nm, respectively. This range covers the typical

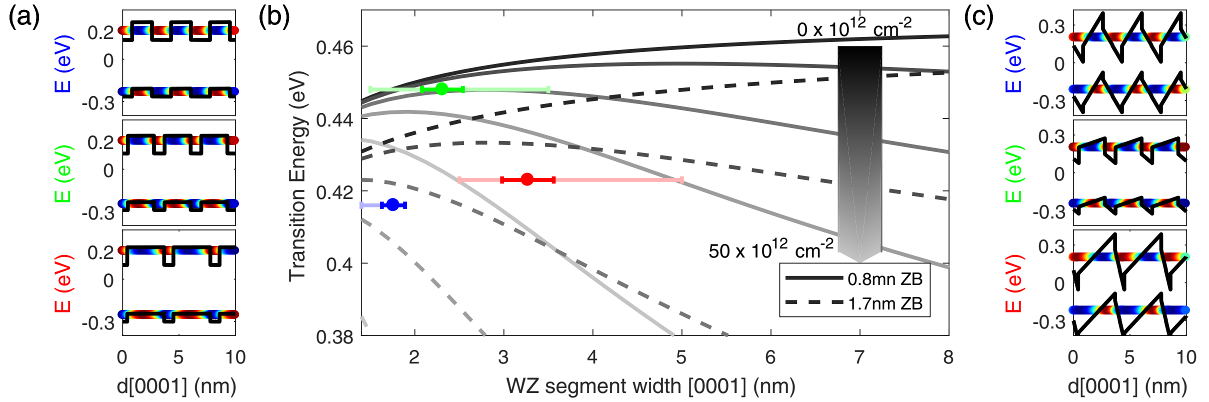


FIG. 6. (a) Idealized conduction-band (CB) and valence-band (VB) profiles, i.e., without polarization sheet charges, for the three different WZ/ZB polytype SL structures (samples A, B, C) using the averaged WZ/ZB-stacking lengths as defined in Table I. The squared wave functions for electron and hole ground states are depicted with color codes (red/blue: highest/lowest intensity). (b) Calculated optical transition energies between CB and VB ground states mapped as a function of WZ segment length and two different ZB segment lengths (solid versus dashed curves) at 75 K. Each data set depicts also different polarization sheet charge densities, i.e., 0 (black), $1\times10^{13}$ (0.016 C/m, dark grey), $2\times10^{13}$ (0.032 C/m, medium grey), $3\times10^{13}$ (0.048 C/m, grey), and $5\times10^{13}$ cm$^{-2}$ (0.08 C/m) (light grey). The data points (in color) indicate the experimentally observed PL peak energies at 75 K at low excitation power. The error bars delineate the standard deviation from the average WZ segment length obtained from statistical analysis as well as the typical minimum and maximum segment lengths observed in these samples. (c) CB and VB profiles and respective electron and hole ground states for the three different SL structures, assuming the presence of polarization sheet charges, that give closest agreement to the experimental PL peak energies; used values for the polarization sheet charges are 0.04, 0.014, and 0.063 C/m for $T^{\mathrm{G}} = 430\,^{\circ}$C, 490 °C, and 530 °C, respectively.

segment lengths in the present polytypic InAs NWs as observed by TEM. Note that for the ZB segment length, we selected these specific values, because the maximum ZB segment lengths observed in the NWs grown at high temperature do not exceed ~1 nm, while those seen in NWs grown at low temperature are also less than ~2 nm wide (see Table I).

Figure 6(b) plots the calculated transition energies as a function of WZ segment length for the two corresponding ZB segment lengths (0.8 nm, 1.7 nm). The plot also illustrates the change in transition energy mediated by different polarization sheet charges in the range of $1\times10^{13}$ cm$^{-2}$ (0.016 C/m) to $5\times10^{13}$ cm$^{-2}$ (0.08 C/m). We also performed calculations for smaller polarization sheet charges ($1\times10^{11}$–$5\times10^{12}$ cm$^{-2}$), but do not plot the respective data since the values are too close to the data without polarization sheet charge (black curves). The simulated polarization sheet charge densities are within the range of recently reported densities [28,31]. Several important trends can be observed. First, and irrespective of the WZ segment length, the calculated data show that the transition energy is more blueshifted to higher energies with decreasing ZB segment length, due to the stronger confinement potential in thinner ZB segments. For example, for the case without polarization, the transition energy is at least by more than 10 meV blueshifted when the ZB segment length is decreased from 1.7 to 0.8 nm (compare black dashed curves). Note that the strength of the confinement potential is mainly governed by the electrons confined in the ZB inclusions, rather than the holes in the WZ segments, since the electron effective mass in InAs is significantly smaller than the hole effective mass [40]. This is also evidenced by the fact that the transition energy does not change much for increased WZ segment lengths (e.g., $>\sim$3 nm), best seen for the case without polarization. Secondly, the polarization sheet charge has a huge influence on the transition energy, yielding a rapid decrease in transition energy above a sheet charge density of $>10^{13}$ cm$^{-2}$. This is due to the fact that the internal electrostatic fields alter the CB and VB profiles, leading to sawtoothlike profiles as shown in Fig. 6(c), which reduces the confinement potential [76].

To provide a comparison between the calculated transition energies and the experimental data, Fig. 6(b) also plots the observed PL peak energies for the three investigated NW samples. Note, that for best comparison the PL peak energies plotted here stem from low excitation power conditions (0.35 mW), which are shifted by ~-10 meV with respect to those shown in Fig. 2(d) due to the absence of band filling. In addition, the data points illustrate also the microscopic variations of the nonperiodic WZ/ZB structure as marked by the horizontal error bars. While the high-contrast error bars give the average WZ segment length, the low-contrast error bars delineate the range of WZ segment lengths observed in each sample. This is relevant because stacking sequences with longer periodicities in a given sample, i.e., regions with longest ZB and WZ segment length, correspond to the lowest recombination energies, which are most sensitive to the PL [73]. Direct comparison clearly shows that polarization sheet charges need to be taken into account to best describe the experimental data. For example, for sample B ($T^{\mathrm{G}} = 490\,^{\circ}$C), the data suggest that a polarization sheet charge density close to $\sim1\times10^{13}$ cm$^{-2}$ fits best to the experimental data. For the other samples A and C, slightly larger polarization sheet charge densities of $\sim2$–$3\times10^{13}$ and $\sim3-5\times10^{13}$ cm$^{-2}$ are required to obtain the best match with the experimental data. As these polarization sheet charge densities are within the range of reported densities [28,31], the employed 1D Kronig-Penney type model provides a sufficiently reasonable approximation of the experimental PL peak energies. Figure 6(c) further illustrates the respective CB and VB profiles and electron and hole ground states for the modelled SL structures with

polarization sheet charges that give closest agreement to the experimental PL peak energies.

In order to explain the higher polarization sheet charge densities for samples A and C, we consider the following. For sample A ($T^{G} = 430\,^{\circ}$C), which contains a much larger fraction of ZB phase and more frequent WZ/ZB stacking sequences, it is likely that in addition to spontaneous polarization given by the WZ segments also a strain-mediated piezoelectric polarization becomes relevant. This scenario is fairly realistic, considering recent experimental investigations, which suggest that InAs NWs with heavy ZB/WZ intermixing experience higher internal strain as opposed to NWs, that are more WZ-dominated [77]. On the other hand, in the limit of WZ-dominated InAs NWs that contain SFs and hence only very narrow ZB inclusions (sample C, $T^{G} = 530\,^{\circ}$C), the total polarization sheet charge is expected to be dominated by contributions from the spontaneous polarization field rather than piezoelectric polarization sheet charges. Spontaneous polarization sheet charges in excess of $>10^{13}$ cm$^{-3}$ have indeed been observed experimentally in WZ-dominated InAs NWs [28,31]. However, the lower number of ZB inclusions is also expected to reduce the internal strain, which may also partially contribute to the reduction in the PL peak energy, and, thus, the observed effect may not be ascribed to the polarization field alone. Recent Raman spectroscopy experiments confirmed that for lower number of ZB segments and SFs in otherwise WZ-phase NWs, the compressive strain component is decreased [77], which induces a reduced effective energy gap and hence may contribute partially to the redshift in PL emission. Since we do not have direct measurement data of the internal strain arising from the WZ/ZB phase intermixing, we do not wish to overstress the discussion on the nature of the polarization sheet charge at this point. In summary, though, the calculated optical transition energies provide a very useful description of the experimental trends observed in PL energy shifts with different WZ/ZB stacking and might be suitable for also testing other III-V NWs with crystal-phase intermixing.

## V. SUMMARY

In this study, we investigated the carrier trapping and thermal activation behavior in polytypic InAs NWs composed of random and short-period wurtzite (WZ)-zincblende (ZB) stacking. Although the short-period intermixing of WZ and ZB layers is a direct consequence of the noncatalytic (droplet-free) growth of the [0001]-oriented InAs NWs, we found that the fractions of WZ and ZB inclusions as well as associated stacking faults are tunable by growth temperature. Higher growth temperatures lead to a higher WZ fraction and extended WZ segment lengths as observed by high-resolution transmission electron microscopy, irrespective of the diameter of the NWs. The effect of different short-period WZ/ZB stacking was studied with respect to the optical transition energies by temperature-dependent micro-photoluminescence ($\mu$PL). We recognized that as the microstructure of the NWs changes from very short ($\sim$1.5 nm wide) WZ/ZB stacking sequences to more well-defined crystal-phase boundaries with WZ segment length $>2$ nm, the low-temperature PL peak energies rise from $\sim$0.42 eV to $\sim$0.45 eV and then decrease again to $\sim$0.43 eV for even larger WZ segment length ($\sim$3–4 nm). To understand the experimental trends in PL emission energies, we proposed model calculations of the optical transition energies as a function of different WZ/ZB stacking sequences by approximating the structure of our InAs NWs by short-period WZ/ZB-type SLs using a simple effective mass approximation (Kronig-Penney type model). The model suggests that reasonable coincidence between the calculated and experimental data is achieved, when taking spontaneous and piezoelectric polarization sheet charges into account which occur at the WZ/ZB interfaces.

The carrier confinement and activation processes at the WZ/ZB interfaces were further found to obey the same thermal characteristics in both $\mu$PL and 4T-NW-FET measurements of the carrier conductivity. The latter illustrated that the carrier density is activated from $\sim10^{16}$ to $\sim10^{17}$ cm$^{-3}$ with increasing temperature, following a two-step activation process. Our analysis suggests that at low temperature the process is driven by activation from the WZ/ZB-related traps, which is also confirmed by the activation behavior found from the temperature-dependent PL peak shifts. On the other hand, at high temperature, a second activation process occurs, which we attribute to activation from surface states and related electron accumulation at the InAs NW surface. This assignment was confirmed by NW diameter dependent investigations, where larger apparent activation energies in thinner NWs illustrate the increased effect of surface state defects to the transport. In summary, our combined approach using optical and electrical transport spectroscopy has proven instructive to discriminate different carrier traps and their different activation behavior, and may also serve to probe other III-V NW systems with rich structural features.

## ACKNOWLEDGMENTS

The authors thank S. Birner (Nextnano GmbH) for helpful discussions with simulations, as well as M. Bichler and H. Riedl for experimental support. We also acknowledge funding by the German Excellence Initiative via the program "Nanosystems Initiative Munich (NIM)," and the German Research Foundation (DFG) via DFG-project KO-4005/5-1. Further support was provided by the Technische Universität München, Institute for Advanced Study (IAS-TUM) as well as the International Graduate School for Science and Engineering (IGSSE-TUM).

[1] T. Akiyama, K. Sano, K. Nakamura, and T. Ito, Jpn. J. Appl. Phys. **45**, L275 (2006).

[2] F. Glas, J.-C. Harmand, and G. Patriarche, Phys. Rev. Lett. **99**, 146101 (2007).

[3] P. Krogstrup, R. Popovitz-Biro, E. Johnson, M. H. Madsen, J. Nygard, and H. Shtrikman, Nano Lett. **10**, 4475 (2010).

[4] H. Joyce, J. Wong-Leung, Q. Gao, H. H. Tan, and C. Jagadish, Nano Lett. **10**, 908 (2010).

[5] T. T. T. Vu, T. Zehender, M. A. Verheijen, S. R. Plissard, G. W. G. Immink, J. E. M. Haverkort, and E. P. A. M. Bakkers, Nanotechnol. **24**, 115705 (2013).

[6] S. Assali, I. Zardo, S. Plissard, D. Kriegner, M. A. Verheijen, G. Bauer, A. Meijerink, A. Belabbes, F. Bechstedt, J. E. M. Haverkort, and E. P. A. M. Bakkers, Nano Lett. **13**, 1559 (2013).

[7] D. Spirkoska, J. Arbiol, A. Gustafsson, S. Conesa-Boj, F. Glas, I. Zardo, M. Heigoldt, M. H. Gass, A. L. Bleloch, S. Estrade, M. Kaniber, J. Rossler, F. Peiro, J. R. Morante, G. Abstreiter, L. Samuelson, and A. Fontcuberta i Morral, Phys. Rev. B **80**, 245325 (2009).

[8] K. A. Dick, P. Caroff, J. Bolinsson, M. E. Messing, J. Johansson, K. Deppert, L. R. Wallenberg, and L. Samuelson, Semicond. Sci. Technol. **25**, 024009 (2010).

[9] K. Ikejiri, Y. Kitauchi, K. Tomioka, J. Motohisa, and T. Fukui, Nano Lett. **11**, 4314 (2011).

[10] S. Morkötter, S. Funk, M. Liang, M. Döblinger, S. Hertenberger, J. Treu, D. Rudolph, A. Yadav, J. Becker, M. Bichler, G. Scarpa, P. Lugli, I. Zardo, J. J. Finley, G. Abstreiter, and G. Koblmüller, Phys. Rev. B **87**, 205303 (2013).

[11] J. Bao, D. C. Bell, F. Capasso, J. B. Wagner, T. Martensson, J. Trägardh, and L. Samuelson, Nano Lett. **8**, 836 (2008).

[12] K. Pemasiri, M. Montazeri, R. Gass, L. M. Smith, H. E. Jackson, J. Yarrison-Rice, S. Paiman, Q. Gao, H. H. Tan, C. Jagadish, X. Zhang, and J. Zou, Nano Lett. **9**, 648 (2009).

[13] J. Wallentin, K. Mergenthaler, M. Ek, L. R. Wallenberg, L. Samuelson, K. Deppert, M.-E. Pistol, and M. T. Borgström, Nano Lett. **11**, 2286 (2011).

[14] H. J. Joyce, J. Wong-Leung, C.-K. Yong, C. J. Docherty, S. Paiman, Q. Gao, H. H. Tan, C. Jagadish, J. Lloyd-Hughes, L. M. Herz, and M. B. Johnston, Nano Lett. **12**, 5325 (2012).

[15] M. Möller, M. M. de Lima Jr, A. Cantarero, T. Chiaramonte, M. A. Cotta, and F. Iikawa, Nanotechnol. **23**, 375704 (2012).

[16] M. Murayama and T. Nakayama, Phys. Rev. B **49**, 4710 (1994).

[17] N. Akopian, G. Patriarche, L. Liu, J.-C. Harmand, and V. Zwiller, Nano Lett. **10**, 1198 (2010).

[18] N. Vainorius, S. Lehmann, D. Jacobsson, L. Samuelson, K. A. Dick, and M. E. Pistol, Nano Lett. **15**, 2652 (2015).

[19] B. Loitsch, J. Winnerl, G. Grimaldi, J. Wierzbowski, D. Rudolph, S. Morkötter, M. Döblinger, G. Abstreiter, G. Koblmüller, and J. J. Finley, Nano Lett. **15**, 7544 (2015).

[20] C. Thelander, P. Caroff, S. Plissard, A. W. Dey, and K. A. Dick, Nano Lett. **11**, 2424 (2011).

[21] T. Bryllert, L.-E. Wernersson, L. E. Froberg, and L. Samuelson, IEEE Electron Dev. Lett. **27**, 323 (2006).

[22] K. E. Moselund, H. Schmid, C. Bessire, M. T. Björk, H. Ghoneim, and H. Riel, IEEE Electron Dev. Lett. **33**, 1453 (2012).

[23] Y.-J. Doh, J. A. van Dam, A. L. Roest, E. P. A. M. Bakkers, L. P. Kouwenhoven, and S. De Franceschi, Science **309**, 272 (2005).

[24] S. Chuang, Q. Gao, R. Kapadia, A. C. Ford, J. Guo, and A. Javey, Nano Lett. **13**, 555 (2013).

[25] M. Nilsson, L. Namazi, S. Lehmann, M. Leijnse, K. A. Dick, and C. Thelander, Phys. Rev. B **93**, 195422 (2016).

[26] M. Hjort, S. Lehmann, J. Knutsson, A. A. Zakharov, Y. A. Du, S. Sakong, R. Timm, G. Nylund, E. Lundgren, P. Kratzer, K. A. Dick, and A. Mikkelsen, ACS Nano **8**, 12346 (2014).

[27] A. Belabbes, C. Panse, J. Furthmüller, and F. Bechstedt, Phys. Rev. B **86**, 075208 (2012).

[28] S. A. Dayeh, D. Susac, K. L. Kavanagh, E. T. Yu, and D. Wang, Adv. Funct. Mater. **19**, 2102 (2009).

[29] A. Belabbes, J. Furthmüller, and F. Bechstedt, Phys. Rev. B **87**, 035305 (2013).

[30] I.-J. Chen, S. Lehmann, M. Nilsson, P. Kivisaari, H. Linke, K. A. Dick, and C. Thelander, Nano Lett. **17**, 902 (2017).

[31] L. Li, Z. Gan, M. R. McCartney, H. Liang, H. Yu, W.-J. Yin, Y. Yan, Y. Gao, J. Wang, and D. J. Smith, Adv. Mater. **26**, 1052 (2014).

[32] S. A. Dayeh, E. T. Yu, and D. Wang, Small **5**, 77 (2009).

[33] V. Schmidt, P. F. J. Mensch, S. F. Karg, B. Gotsmann, P. Das Kanungo, H. Schmid, and H. Riel, Appl. Phys. Lett. **104**, 012113 (2014).

[34] C. Thelander, K. A. Dick, M. T. Borgström, L. E. Fröberg, P. Caroff, H. A. Nilsson, and L. Samuelson, Nanotechnol. **21**, 205703 (2010).

[35] K. Sladek, A. Winden, S. Wirths, K. Weis, C. Blömers, Ö. Gül, T. Grap, S. Lenk, M. von der Ahe, T.E. Weirich, H. Hardtdegen, M.I. Lepsa, A. Lysov, Z.-A. Li, W. Prost, F.-J. Tegude, H. Lüth,T. Schäpers, and D. Grützmacher, Phys. Stat. Sol. C **9**, 230 (2012).

[36] A. R. Ullah, H. J. Joyce, A. M. Burke, H. H. Tan, C. Jagadish, and A. P. Micolich, Phys. Stat. Sol. RRL **7**, 911 (2013).

[37] C. Blömers, T. Rieger, T. Grap, M. Raux, M. I. Lepsa, H. Lüth, D. Grützmacher, and T. Schäpers, Nanotechnology **24**, 325201 (2013).

[38] V. E. Degtyarev, S. V. Khazanova, and N. V. Demarina, Sci. Rep. **7**, 3411 (2017).

[39] M. J. L. Sourribes, I. Isakov, M. Panfilova, H. Liu, and P. A. Warburton, Nano Lett. **14**, 1643 (2014).

[40] G. Koblmüller, K. Vizbaras, S. Hertenberger, S. Bolte, D. Rudolph, J. Becker, M. Döblinger, M-C. Amann, J. J. Finley, and G. Abstreiter, Appl. Phys. Lett. **101**, 053101 (2012).

[41] E. Dimakis, J. Lähnemann, U. Jahn, S. Breuer, M. Hilse, L. Geelhaar, and H. Riechert, Cryst. Growth Des. **11**, 4001 (2011).

[42] C. Blömers, T. Grap, M. I. Lepsa, J. Moers, S. Trellenkamp, D. Grützmacher, H. Lüth, and T. Schäpers, Appl. Phys. Lett. **101**, 152106 (2012).

[43] S. Hertenberger, D. Rudolph, S. Bolte, M. Döblinger, M. Bichler, D. Spirkoska, J. J. Finley, G. Abstreiter, and G. Koblmüller, Appl. Phys. Lett. **98**, 123114 (2011).

[44] S. Hertenberger, D. Rudolph, J. Becker, M. Bichler, J. J. Finley, G. Abstreiter, and G. Koblmüller, Nanotechnol. **23**, 235602 (2012).

[45] D. R. Khanal and J. Wu, Nano Lett. **7**, 2778 (2007).

[46] P. Caroff, J. Bolinsson, and J. Johansson, Select. IEEE J. Top. Quant. Electron. **17**, 829 (2011).

[47] D. Kriegner, C. Panse, B. Mandl, K. A. Dick, M. Keplinger, J. M. Persson, P. Caroff, D. Ercolani, L. Sorba, F. Bechstedt, J. Stangl, and G. Bauer, Nano Lett. **11**, 1483 (2011).

[48] D. N. Zakharov, Z. Liliental-Weber, B. Wagner, Z. J. Reitmeier, E. A. Preble, and R. F. Davis, Phys. Rev. B **71**, 235334 (2005).

[49] K. Tomioka, J. Motohisa, S. Hara, and T. Fukui, Jpn. J. Appl. Phys. **46**, L1102 (2007).

[50] J. Johannson, K. A. Dick, P. Caroff, M. E. Messing, J. Bolinsson, K. Deppert, and L. Samuelson, J. Phys. Chem. C **114**, 3837 (2010).

[51] H. Shtrikman, R. Popovitz-Biro, A. Kretinin, L. Houben, M. Heiblum, M. Bukala, M. Galicka, R. Buczko, and P. Kacman, Nano Lett. **9**, 1506 (2009).

[52] J. Johannson, L. S. Karlsson, C. P. T. Svensson, T. Mårtensson, B. A. Wacaser, K. Deppert, L. Samuelson, and W. Seifert, Nat. Mater. **5**, 574 (2006).

[53] V. G. Dubrovskii, N. V. Sibirev, J. C. Harmand, and F. Glas, Phys. Rev. B **78**, 235301 (2008).
[54] D. Jacobsson, F. Panciera, J. Tersoff, M. C. Reuter, S. Lehmann, S. Hofmann, K. A. Dick, and F. M. Ross, Nature **531**, 317 (2016).
[55] T. Yamashita, T. Akiyama, K. Nakamura, and T. Ito, Jpn. J. Appl. Phys. **50**, 055001 (2011).
[56] K. Ikejiri, T. Sato, H. Yoshida, K. Hiruma, J. Motohisa, S. Hara, and T. Fukui, Nanotechnology **19**, 265604 (2008).
[57] Z. Zanolli, F. Fuchs, J. Furthmüller, U. von Barth, and F. Bechstedt, Phys. Rev. B **75**, 245121 (2007).
[58] Y. Varshni, Physica **34**, 149 (1967).
[59] A. M. Graham, P. Corfdir, M. Heiss, S. Conesa-Boj, E. Uccelli, A. Fontcuberta i Morral, and R. T. Phillips, Phys. Rev. B **87**, 125304 (2013).
[60] D. M. Irber, J. Seidl, D. J. Carrad, J. Becker, N. Jeon, B. Loitsch, J. Winnerl, S. Matich, M. Döblinger, Y. Tang, S. Morkötter, G. Abstreiter, J. J. Finley, M. Grayson, L. J. Lauhon, and G. Koblmüller, Nano Lett. **17**, 4886 (2017).
[61] O. Wunnicke, Appl. Phys. Lett. **89**, 083102 (2006).
[62] M. Scheffler, S. Nadj-Perge, L. P. Kouwenhoven, M. T. Borgström, and E. P. A. M. Bakkers, J. Appl. Phys. **106**, 124303 (2009).
[63] S. Wirths, K. Weis, A. Winden, K. Sladek, C. Volk, S. Alagha, T. E. Weirich, M. von der Ahe, H. Hardtdegen, H. Lüth, N. Demarina, D. Grützmacher, and Th. Schäpers, J. Appl. Phys. **110**, 053709 (2011).
[64] N. Mott, Rev. Mod. Phys. **40**, 677 (1968).
[65] M. Speckbacher, J. Treu, T. J. Whittles, W. M. Linhart, X. Xu, K. Saller, V. R. Dhanak, G. Abstreiter, J. J. Finley, T. D. Veal, and G. Koblmüller, Nano Lett. **16**, 5135 (2016).
[66] J. R. Weber, A. Janotti, and C. G. Van de Walle, Appl. Phys. Lett. **97**, 192106 (2010).
[67] A. Konar, J. Mathew, K. Nayak, M. Bajaj, R. K. Pandey, S. Dhara, K. V. R. M. Murali, and M. M. Deshmukh, Nano Lett. **15**, 1684 (2015).
[68] J. Treu, M. Bormann, H. Schmeiduch, M. Döblinger, S. Morkötter, S. Matich, P. Wiecha, K. Saller, B. Mayer, M. Bichler, M.-C. Amann, J. J. Finley, G. Abstreiter, and G. Koblmüller, Nano Lett. **13**, 6070 (2013).
[69] B. T. Meggitt, E. H. C. Parker, and R. M. King, Appl. Phys. Lett. **33**, 528 (1978).
[70] S. P. Watkins, C. A. Tran, R. Ares, and G. Soerensen, Appl. Phys. Lett. **66**, 882 (1995).
[71] E. S. Hwang, E. M. Park, E.-K. Suh, C.-H. Hong, H. J. Lee, X. Q. Wang, Y. Ishitani, and A. Yoshikawa, J. Korean Phys. Soc. **49**, 1530 (2006).
[72] N. Ma, X. Q. Wang, S. T. Liu, L. Feng, G. Chen, F. J. Xu, N. Tang, L. W. Lu, and B. Shen, Appl. Phys. Lett. **99**, 182107 (2011).
[73] M. Heiss, S. Conesa-Boj, J. Ren, H.-H. Tseng, A. Gali, A. Rudolph, E. Uccelli, F. Peiro, J. R. Motante, D. Schuh, E. Reiger, E. Kaxiras, J. Arbiol, and A. Fontcuberta i Morral, Phys. Rev. B **83**, 045303 (2011).
[74] S. Birner, T. Zibold, T. Andlauer, T. Kubis, M. Sabathil, A. Trellakis, and P. Vogl, IEEE Trans. Electron. Dev. **54**, 2137 (2007).
[75] G. Bastard, E. E. Mendez, L. L. Chang, and L. Esaki, Phys. Rev. B **26**, 1974 (1982).
[76] J. Lähnemann, O. Brandt, U. Jahn, C. Pfüller, C. Roder, P. Dogan, F. Grosse, A. Belabbes, F. Bechstedt, A. Trampert, and L. Geelhaar, Phys. Rev. B **86**, 081302(R) 2012.
[77] J. K. Panda, A. Roy, A. Chakraborty, I. Dasgupta, E. Hasanu, D. Ercolani, L. Sorba, and M. Gemmi, Phys. Rev. B **92**, 205302 (2015).